Global precipitation measuring dual-frequency precipitation radar observations of hailstorm vertical structure: Current capabilities and drawbacks

Original
Global precipitation measuring dual-frequency precipitation radar observations of hailstorm vertical structure: Current capabilities and drawbacks / Mroz, K., Battaglia, A., Lang, T.J., Tanelli, S., Sacco, G.F.. - In: JOURNAL OF APPLIED METEOROLOGY AND CLIMATOLOGY. - ISSN 1558-8424. - 57:9(2018), pp. 2161-2178. [10.1175/JAMC-D-18-0020.1]

Publisher:
American Meteorological Society

Published
DOI:10.1175/JAMC-D-18-0020.1

SPECIAL
Global Precipitation Measurement (GPM)
COLLECTION

Global Precipitation Measuring Dual-Frequency Precipitation Radar Observations of Hailstorm Vertical Structure: Current Capabilities and Drawbacks

KAMIL MROZ

National Centre for Earth Observation, University of Leicester, Leicester, United Kingdom

ALESSANDRO BATTAGLIA

Earth Observation Science, Department of Physics and Astronomy, and National Centre for Earth Observation,
University of Leicester, Leicester, United Kingdom

TIMOTHY J. LANG

National Aeronautics and Space Administration Marshall Space Flight Center, Huntsville, Alabama

SIMONE TANELLI AND GIAN FRANCO SACCO

Jet Propulsion Laboratory, California Institute of Technology, Pasadena, California

(Manuscript received 19 January 2018, in final form 11 July 2018)

ABSTRACT

A statistical analysis of simultaneous observations of more than 800 hailstorms over the continental United States performed by the Global Precipitation Measurement (GPM) Dual-Frequency Precipitation Radar (DPR) and the ground-based Next Generation Weather Radar (NEXRAD) network has been carried out. Several distinctive features of DPR measurements of hail-bearing columns, potentially exploitable by hydrometeor classification algorithms, are identified. In particular, the height and the strength of the Ka-band reflectivity peak show a strong relationship with the hail shaft area within the instrument field of view (FOV). Signatures of multiple scattering (MS) at the Ka band are observed for a range of rimed particles, including but not exclusively for hail. MS amplifies uncertainty in the effective Ka reflectivity estimate and has a negative impact on the accuracy of dual-frequency rainfall retrievals at the ground. The hydrometeor composition of convective cells presents a large inhomogeneity within the DPR FOV. Strong nonuniform beamfilling (NUBF) introduces large ambiguities in the attenuation correction at Ku and Ka bands, which additionally hamper quantitative retrievals. The effective detection of profiles affected by MS is a very challenging task, since the inhomogeneity within the DPR FOV may result in measurements that look remarkably like MS signatures. The shape of the DPR reflectivity profiles is the result of the complex interplay between the scattering properties of the different hydrometeors, NUBF, and MS effects, which significantly reduces the ability of the DPR system to detect hail at the ground.

1. Introduction

The launch of the Global Precipitation Measurement (GPM) mission core satellite in February 2014 offers an unprecedented opportunity to explore the three-dimensional structure of precipitating systems from space (Hou et al. 2014). The mission carries on the legacy of the Tropical Rainfall Measuring Mission (TRMM), thoroughly described by Kummerow et al. (1998), with the goals of mapping global precipitation and of better understanding the structure of precipitating systems. Among them, thunderstorms are certainly

---

Denotes content that is immediately available upon publication as open access.

Corresponding author: Kamil Mroz, km357@le.ac.uk

DOI: 10.1175/JAMC-D-18-0020.1

the most destructive and fascinating weather elements. The detection of hail cores within convective regions of different types of thunderstorms (single cells, multicell clusters, squall lines, and supercells) has already been the subject of many studies, for example, Donaldson (1959), Waldvogel et al. (1979), Auer (1994), Kitzmiller et al. (1995), Witt et al. (1998), Heinselman and Ryzhkov (2006), Depue et al. (2007), Cecil (2011), Cecil and Blankenship (2012), and Ortega et al. (2016).

TRMM observations have already shed light on where the most intense thunderstorms occur and what their microwave radiometer and Ku-band radar footprints are (Zipser et al. 2006). Because of the high single-scattering albedo of ice particles, passive microwave radiometers feature large brightness temperature depressions corresponding to large amounts of ice (Cecil 2011; Cecil and Blankenship 2012). The most extreme storm in the TRMM dataset was captured on 30 December 1997 in northern Argentina (Zipser et al. 2006). Within its extent, an astonishing brightness temperature of 69 K at 37 GHz was measured. Moreover, even a lower-frequency channel (19 GHz) bore the hallmarks of scattering because of large hailstones (a brightness temperature below 150 K). During the GPM era, another exceptionally intense hailstorm was observed over the Mediterranean Sea. It was characterized by brightness temperatures of 89 and 159 K at 36.5- and 19-GHz channels (Marra et al. 2017), respectively.

In the past decade, several studies (Cecil 2009, 2011; Cecil and Blankenship 2012; Ferraro et al. 2015; Mroz et al. 2017; Ni et al. 2017) have tried to identify thresholds of brightness temperatures at the different frequencies for the detection of hail embedded in a precipitating system identified by a precipitation feature (Nesbitt et al. 2000), that is, contiguous areas occupied by clouds and rain. Such measurements can then be combined with ground validation to statistically establish optimal detection thresholds. Some authors have used hail reports at the ground and matched them with the precipitation features by using some time- and range-constraint criteria. This approach has been applied to TRMM data first (Cecil 2011; Cecil and Blankenship 2012) and more recently to GPM data (Ni et al. 2017). Other authors (Leppert and Cecil 2015) have used hydrometeor classification algorithms based on polarimetric S-band measurements, which identify the presence of hail in three-dimensional volumes. Similarly, by exploiting observations from polarimetric ground-based radars, Mroz et al. (2017) proposed a pixel-based hail-detection algorithm tailored to GPM observables. The algorithm only detects hail-contaminated columns without ranging the position of hail cores and therefore with no attempt of detecting cases where hail is reaching the ground.

The goal of this work is to identify and characterize Dual-Frequency Precipitation Radar (DPR) observations of hail-bearing profiles with a specific focus on assessing the capabilities in detecting hail at the ground. This represents a very challenging problem because of several factors. First, the interpretation of the dual-frequency ratio (DFR) requires disentangling the ambiguities associated with strong attenuation caused by convective cores. Second, large ice particles aloft act as almost perfect scatterers and tend to enhance multiple scattering (MS), especially at the Ka band (Battaglia et al. 2010, 2015, 2016b). In the most extreme cases, multiple-scattered radiation dominates the Ka-band signal and causes an abnormal shape of the DFR profile similar to a ‘‘knee’’ (Battaglia et al. 2014). Such DFR knees were documented in deep convective systems, which suggest they may be a signature of hail, but a detailed analysis is necessary to validate this hypothesis. Third, the size of the DPR footprint is too large to properly resolve the structure of convective systems. Musil et al. (1991) reported that about half of the observed updraft–downdraft regions for Montana hailstorms were no wider than 1.5–2 km and the largest encountered updraft (downdraft) was 15 (8) km wide. Issues related to nonuniform beamfilling (NUBF) have been thoroughly described by many authors, for example, Kozu and Iguchi (1999), Durden and Tanelli (2008), Meneghini and Liao (2013), and Short et al. (2013, 2015). Fourth, within hail shafts, the melting of hailstones below the freezing level (FL) complicates the identification of the different phases of the hydrometeors in the column.

The following questions are addressed throughout this paper: Are there peculiar signatures of hail presence in the column in DPR measurements? What are these signatures? Is it possible to detect hail fall at the ground with the DPR? What are the major limitations of this instrument for detecting hail?

The paper is organized as follows: Section 2 briefly describes the database used in this study. Section 3 gives a statistical description of DPR measurements of hail-bearing columns, section 4 describes the main challenges in the interpretation of DPR measurements, and the last section concludes the main findings.

2. Database

For this study, collocated data from the Next Generation Weather Radar (NEXRAD) network operating in the United States and from the DPR on board the GPM core satellite are exploited. The spaceborne measured reflectivity profiles are extracted from version 5 (V05) of the level-2A DPR product freely available at the NASA

Precipitation Processing Server (PPS). The DPR provides three-dimensional measurements of the atmosphere at the Ku band (13.6 GHz) and Ka band (35.6 GHz) with a resolution of around 5 km horizontally and 250 m vertically at both channels. The swath of the Ku precipitation radar spans across 245 km, whereas the Ka radar samples only the inner region of 120 km—for more details, see Hou et al. (2014). Within the inner swath, observations are performed synchronously and are matched vertically and horizontally to provide dual-frequency measurements of atmospheric systems.

The ground-based system operates at the S band (3 GHz), sending and receiving signals from vertical/horizontal polarization channels. In addition to polarimetric observables, the fuzzy logic hydrometeor classification [hydrometeor identification (HID)] from Dolan and Rutledge (2009) and Dolan et al. (2013) is utilized here as a "ground truth." The validation of different polarimetric algorithms was performed during field campaigns (e.g., Joint Polarimetric Experiment) or general public surveys (e.g., Severe Hazard Analysis and Verification Experiment) and proved their high effectiveness in detecting hail (Heinselman and Ryzhkov 2006; Depue et al. 2007; Ortega et al. 2009, 2016). Moreover, the rain rates at the native ground-based radar resolution as derived from the polarimetric measurements by applying the CSU_RadarTools algorithm (Bringi and Chandrasekar 2001) are utilized as the ground reference. As it was shown by Ryzhkov and Zrnić (1995), the root-mean-square error of these estimates does not exceed 20% compared to rain gauges, which justifies their usage as a reliable source of rainfall data.

Our database consists of the spaceborne and ground-based measurements of 825 intense weather events captured between April 2014 and December 2017. The month of the occurrence and the location of these storms is shown in Fig. 1. Although the analysis is not exclusively focused at any part of the year, most of the events were detected during the warm season when conditions for the formation of convective storms are more favorable. For this study, we down-select our dataset to only those profiles exceeding the 40-dBZ Ku reflectivity threshold above the ground clutter. The ground-based collocated measurements were acquired within 2.5 min of the GPM overpass. To preserve relatively high vertical resolution of the ground-based measurements, only data from within a 100-km range of the nearest S-band radar are used. The matching procedure results in approximately 374 000 DPR profiles, more than 41 000 out of them exceeding the 40-dBZ measured reflectivity threshold. The range constraint ensures that the bottom of the lowest elevation scans does not exceed 1 km above the ground, but even such restrictive conditions regarding the distance from the ground-based stations result in a vertical resolution of 1.7 km at 100 km for synthetic S-band data, which smooths out finescale features of the reflectivity profiles. Nevertheless, these small reflectivity fluctuations average out in a statistical analysis, so they should not have significant impact on the study of the vertical structure of hail-bearing columns. Unfortunately, low vertical resolution of ground-based measurements may also result in some missed hail detections because of averaging over large volumes. This can positively bias the number of the hail-free profiles.

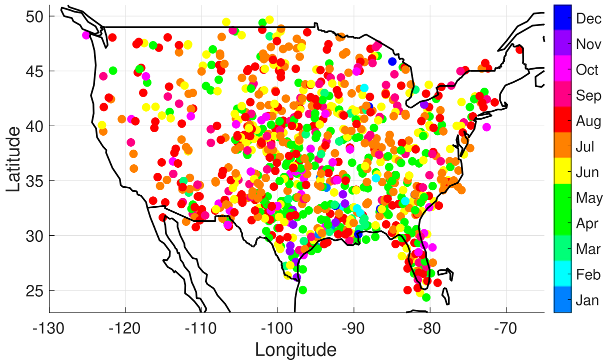

FIG. 1. The location of all intense storms in our dataset of simultaneous measurements performed by the DPR and the NEXRAD network. The month of the storm occurrence is represented by different colors shown in the color bar.

The two observing systems used here have differing spatial resolutions as a result of different scanning geometries. NEXRAD data are characterized by high horizontal resolution, that is, 1° in azimuth and 250 m in range, but only 14 elevation levels are sampled. On the other hand, the spaceborne system samples the atmosphere every 125 m in the vertical direction with a vertical resolution of 250 m, but the footprint of the DPR exceeds 20 km^2. To tackle the disparity in the sampling volumes, a Gaussian approximation of the two-way antenna gain specific for the DPR configuration,

$$G^2(r) \simeq \exp(-8r^2 \ln 2/d_{\mathrm{DPR}}^2), \tag{1}$$

is used to weight and then average the S-band reflectivity in linear units at each elevation scan. In Eq. (1), r denotes the range to the DPR bore sight (not to the ground-based radar); $d_{\mathrm{DPR}} = 5.04$ km is the diameter of the DPR footprint. Then, the resulting synthetic S-band data with 14 levels are linearly interpolated at the DPR vertical resolution. Because of the typical increase of the radar reflectivity with decreasing height, the averaging procedure tends to overestimate S-band reflectivity values at upper levels. However, this deviation should not affect the results because it is not the absolute difference between DPR and ground-based measurements that is the subject of this study. Instead, the relative discrepancies between observations for different hail-contamination are analyzed; thus, biases in ground-based references are less relevant.

By weighting the native-resolution polarimetric hydrometeor classification field with the two-way antenna gain, the fraction of the DPR footprint filled by each hydrometeor type, in particular, hail, can be quantified at each level, as is shown in Fig. 2d. For brevity, the maximal weighted hail fraction in the column is denoted by HF_c; if not explicitly stated, we will refer to it by "hail fraction." Thanks to the use of ground-based measurements only in proximity to NEXRAD radars, we assume that the lowest-elevation scan is representative of the situation at the surface. At the range of 100 km, the bottom of the lowest-elevation scan is about 500 m above the surface according to the 4/3 Earth radius propagation model. Therefore, the part of the DPR field of view (FOV) occupied by hail at the lowest level is considered throughout the paper to be the hail fraction at the ground and is denoted by HF_g. The ground-based rain rate estimates at the lowest-elevation scan are also weighted according to the DPR antenna pattern, and they are used as the reference values.

3. Statistical analysis of hail-bearing DPR profiles

A statistical analysis of DPR profiles within the database of intense weather events has been performed here in order to have a better insight into typical measurements for the hail-affected columns. Note that the analysis is restricted to the DPR columns exceeding 40-dBZ Ku reflectivity value above the surface. No distinction between stratiform and convective rain is done, so profiles with the brightband echo exceeding the given threshold are also included.

a. Statistical ground-based-derived characterization of hail-bearing profiles

The analysis shows that the conditional probability of hail occurrence in the column is very small even for strong Ku reflectivity echoes; that is, approximately 41% of all profiles exceeding the 40-dBZ measured Ku reflectivity threshold have no hail in the column. For 33% of them, hail fraction varies between 0% and 5%, while only 26% of profiles have maximal hail fractions exceeding 5% (approximately 1 km^2); see Fig. 3.

Hereafter, the threshold value of 5% hail fraction in the column ($\mathrm{HF}_c = 5\%$) is used to separate hail-bearing from "hail free" columns in order to exclude false hail detections in the polarimetric hydrometeor classification algorithm that typically appear as isolated hail pixels. The total number of hail-bearing profiles amounts, therefore, to approximately 12 000.

The probability of hail occurrence at the ground is even smaller. This can be attributed to either melting or advection processes or possibly to missed hail detections in HID when hail is mixed with rain within the radar volume. For 74% of hail-bearing profiles, no hail was observed at the ground, and only 9% of them are affected by $\mathrm{HF}_g > 5\%$. As expected, more hail at the surface is observed for lower FLs: only 38%, 22%, 7%, and 1.6% of hail-contaminated profiles have more than 5% of the DPR footprint area affected by hail for FLs of 1–2, 2–3, 3–4, or >4 km above the ground, respectively (Table 1). A majority of low-FL cases are found over the highlands of the Great Plains. Our database does not include a single profile that is uniformly filled by hail at the ground. In fact, no more than 80% of the instrument FOV was ever filled by hail at the ground in our record. This statistic demonstrates the narrow structure of hail shafts with characteristic horizontal sizes smaller than the DPR FOV.

b. DPR observations of the vertical structure of hail-contaminated profiles

The behavior of median reflectivity profiles for different contamination levels is studied throughout this section. The shape of the measured reflectivity profile at the DPR frequencies is mainly driven by two factors: the radar reflectivity of the targets distributed within the beam volume and the signal attenuation along the path. Both of these factors are dependent on the microphysical properties of the observed particles but also on the frequency of the signal. In this section, we show how the hail presence in the column affects measurements underneath hail shafts by comparing DPR observations to synthetic S-band measurements that are subject to much smaller attenuation (Baldini et al. 2012). The database has been stratified according to the hail fraction; for example, no hail ($\mathrm{HF}_c = 0$) and different hail-contamination thresholds, that is, 5%–10%, 10%–15%, 15%–25%, 25%–40%, and 40%–100%. All altitudes are referenced with respect to the freezing level to capture the impact of the melting process.

1) HAIL ONLY ALOFT

First, profiles with no hail at the ground, a freezing level at least 3 km above the ground, and Ku-band reflectivity exceeding 40 dBZ are considered. The median profiles of the DPR measurements for different thresholds of hail contamination are shown in Fig. 4. The shaded area represents the spread between the 25th and 75th percentiles.

The characteristics of DPR measurements for hail-contaminated profiles (blue, green, and red curves) differ significantly from those that are hail free (black),

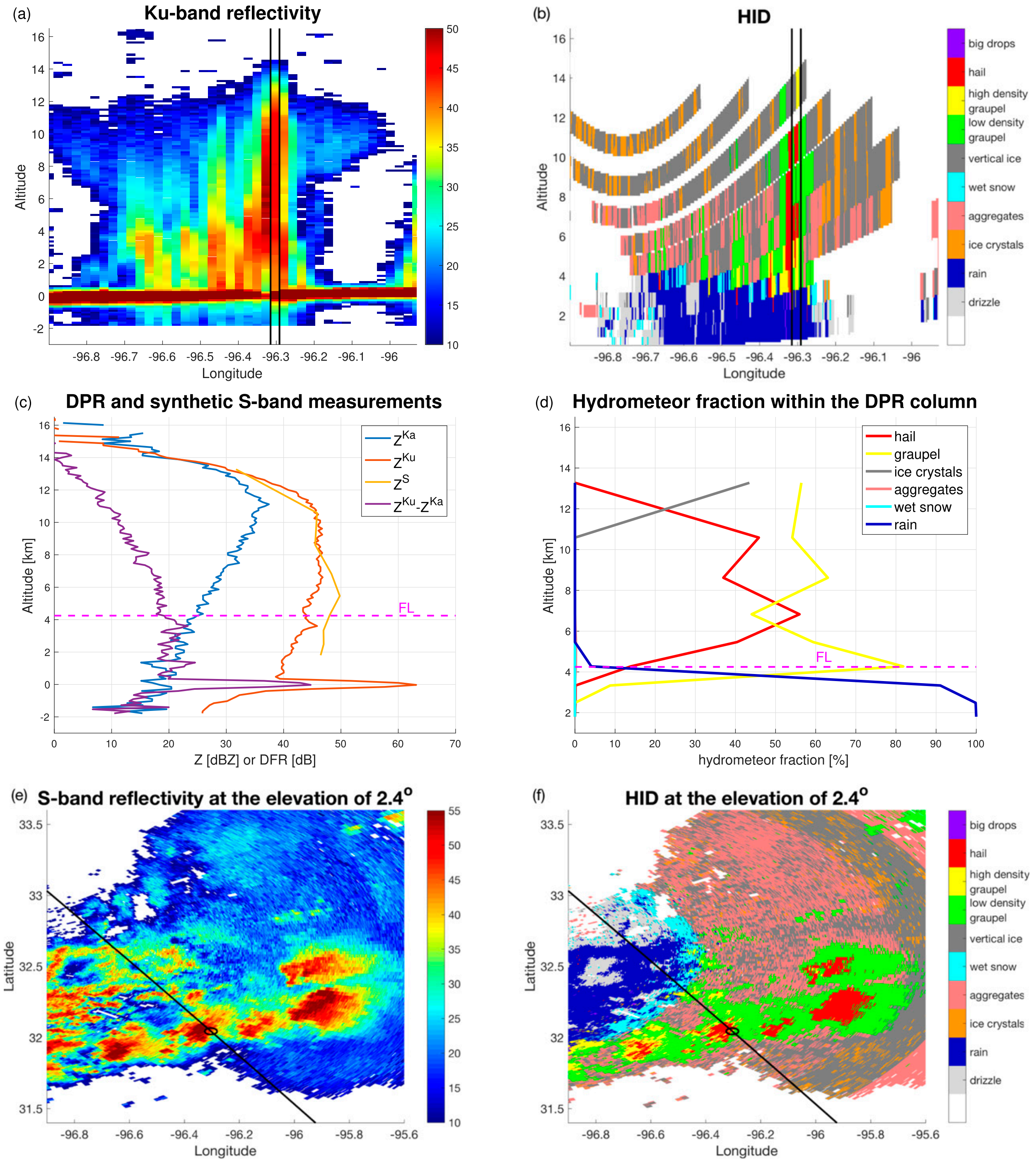

FIG. 2. (a) The Ku-band measurements of the thunderstorm observed by the GPM DPR on 11 May 2015 in the Dallas area. (b) The ground-based HID along the same crosscut. (c) Spaceborne and synthetic S-band measurements corresponding to the vertical column enclosed with the black lines in (a). (d) The hydrometeor composition of the DPR column from (c) as derived from the ground-based polarimetric hydrometeor algorithm. (e) A horizontal crosscut through the S-band reflectivity as measured by the nearest NEXRAD radar (KFWS) at the elevation of 2.4°. (f) The HID field corresponding to the measurements from (e). The black line denotes the location of the cross section from (a) and (b). The black circle shows the DPR footprint area of the profile in (c) and (d).

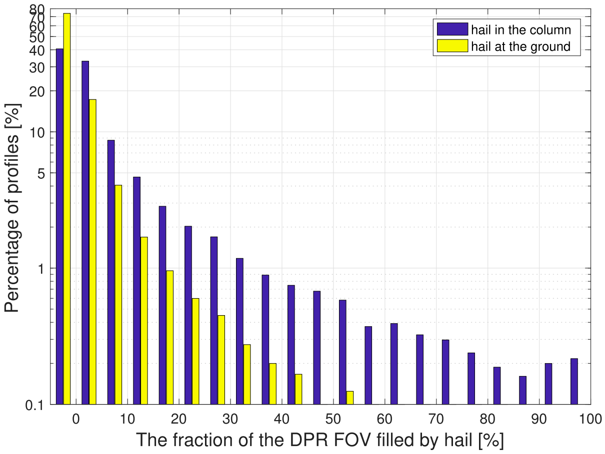

FIG. 3. Histogram of the columnar maximal fraction of the DPR footprint filled by hail for DPR profiles exceeding the measured reflectivity threshold of 40 dBZ at Ku band (blue bars). Histogram of the hail fraction at the lowest elevation (as detected by the ground-based radar) for hail-bearing columns with $\mathrm{HF}_c > 5\%$ (yellow bars). For both histograms, the sample size is equal to approximately 41 000 DPR profiles.

representing 41% of the entire dataset. The peak Ka reflectivity value occurs increasingly higher above the freezing level, and it is stronger with increasing HF_c (Fig. 4a). The slope of the Ka-band profiles of hail-bearing columns does not show any significant change in proximity to the FL, even though such a behavior is expected because of the water-phase transition. Several possible explanations can be presented: first, a high load of heavily rimed particles above the 0°C isotherm induces attenuation comparable to the one caused by rain underneath; second, large amounts of liquid water (essential for the growth and formation of hail) are lifted well above the FL and strongly attenuate the 35-GHz channel there; and third, the MS enhancement dominates the shape of the Ka reflectivity, concealing all the features corresponding to hydrometeor composition, that is, the transition of the water phase.

Similarly, stronger Ku-band reflectivity values are observed higher up in the atmosphere for bigger hail fraction, though the peak reflectivity height is much reduced compared to the Ka-band profile (Fig. 4b). Only for profiles where $\mathrm{HF}_c > 40\%$ does the reflectivity peak more than 1 km higher than the FL, with significant reduction in the measured reflectivity starting from just above the FL downward. The drop in the returned signal may be due to attenuation caused by hailstones and supercooled cloud droplets that are necessary for hail formation. It is also possible that the actual altitude of the FL is higher than the estimate, based on large-scale modeling, because of strong updrafts. In that case, the change in the sloping of the measured reflectivity indicates the “true” transition zone. The reduction in the reflectivity can also be attributed to Mie scattering from dense ice particles comparable to the wavelength of the instrument. Hail-contaminated columns are characterized by steeper Ku reflectivity slopes below the 0°C isotherm for the higher HF_c, which suggests the occurrence of stronger attenuation due to melting hail or heavy rain for wider hail shafts. Indeed, the spatially weighted mean of the rain rates (RRs) derived from the polarimetric measurements for the hail fraction of 5%–10%, 10%–15%, 15%–25%, 25%–40%, and 40%–100% is equal to 18, 20, 22, 24, and 32 mm h^{-1}, respectively, which indicates stronger rain rates for wider convective regions.

TABLE 1. The percentage of hail-bearing columns (the maximal hail fraction in the column exceeds 5% of the DPR field of view) associated with hail fall at the ground larger than 1 km^2. The results are stratified according to the FL height above the surface.

FL height (km)	1–2	2–3	3–4	>4
Fraction of affected profiles (%)	38	22	7	1.6

The median DFR of Ku and Ka reflectivities $\mathrm{DFR}^{\mathrm{Ku}}_{\mathrm{Ka}}$ increases with increasing hail fraction as a result of differential attenuation and non-Rayleigh effects induced by particles comparable to or bigger than Ku and Ka wavelengths (Fig. 4d). For the strongest hail contamination, $\mathrm{DFR}^{\mathrm{Ku}}_{\mathrm{Ka}}$ exceeds 20 dB in proximity of the FL. Moreover, only with the highest hail fraction does the shape of the DFR profile tend to produce a weak DFR knee, which bends at 1 km below the FL. The median DFR value, in proximity to the surface, for profiles with $\mathrm{HF}_c > 40\%$ is smaller than for the other hail-bearing classes, although these profiles are associated with the highest RRs according to the polarimetric algorithm. This is incompatible with the single-scattering theory where differential attenuation produces the highest DFR values for the strongest rain rates. The reduction in the apparent attenuation is evident when the DFR of S- and Ku-band reflectivities $\mathrm{DFR}^{\mathrm{S}}_{\mathrm{Ku}}$ is compared to the DFR of S and Ka data $\mathrm{DFR}^{\mathrm{S}}_{\mathrm{Ka}}$ (Figs. 4b and 4f, respectively). As expected, because of attenuation and Mie effects, $\mathrm{DFR}^{\mathrm{S}}_{\mathrm{Ku}}$ is steadily increasing toward the surface, with the highest values for the strongest hail contamination. Although the same effect is observed for $\mathrm{DFR}^{\mathrm{S}}_{\mathrm{Ka}}$, there is a clear gradient reduction 2 km below the FL for profiles contaminated with hail. This change in the slope of the $\mathrm{DFR}^{\mathrm{S}}_{\mathrm{Ka}}$ can be explained by the multiple-scattering enhancement below hail shafts that compensates part of the attenuation at the Ka band.

To decipher how the hail presence in the column may alter the DPR rain rate retrieval, the median $\mathrm{DFR}^{\mathrm{Ku}}_{\mathrm{Ka}}$ profiles for different rain rates as derived by NEXRAD

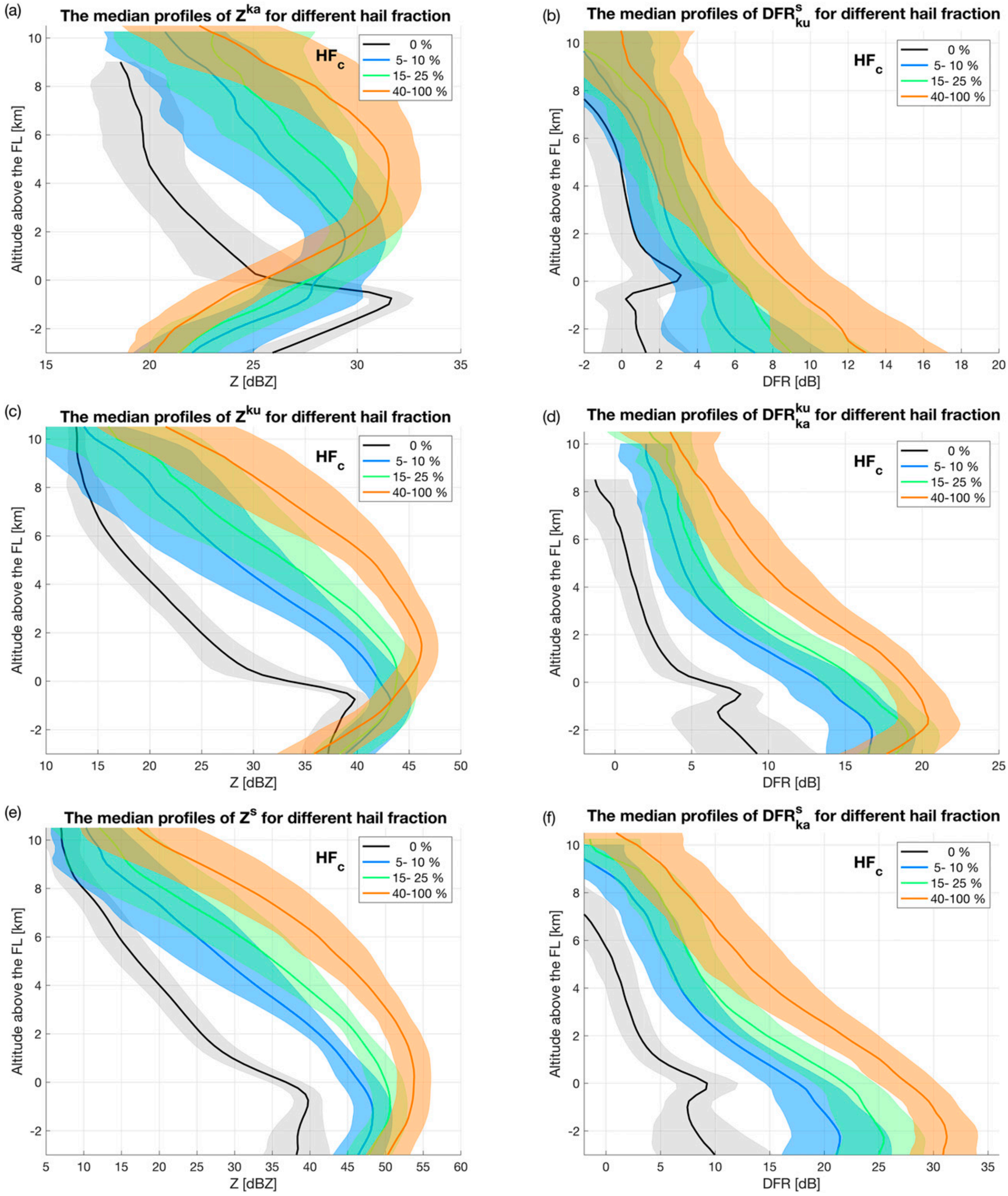

FIG. 4. The median profiles of the DPR observables complemented by the synthetic ground-based data for different hail fractions. The black line represents hail-free columns, whereas the colored lines are associated with different hail-contamination levels (see legend). The semitransparent envelope marks the region between the 25th and 75th percentiles.

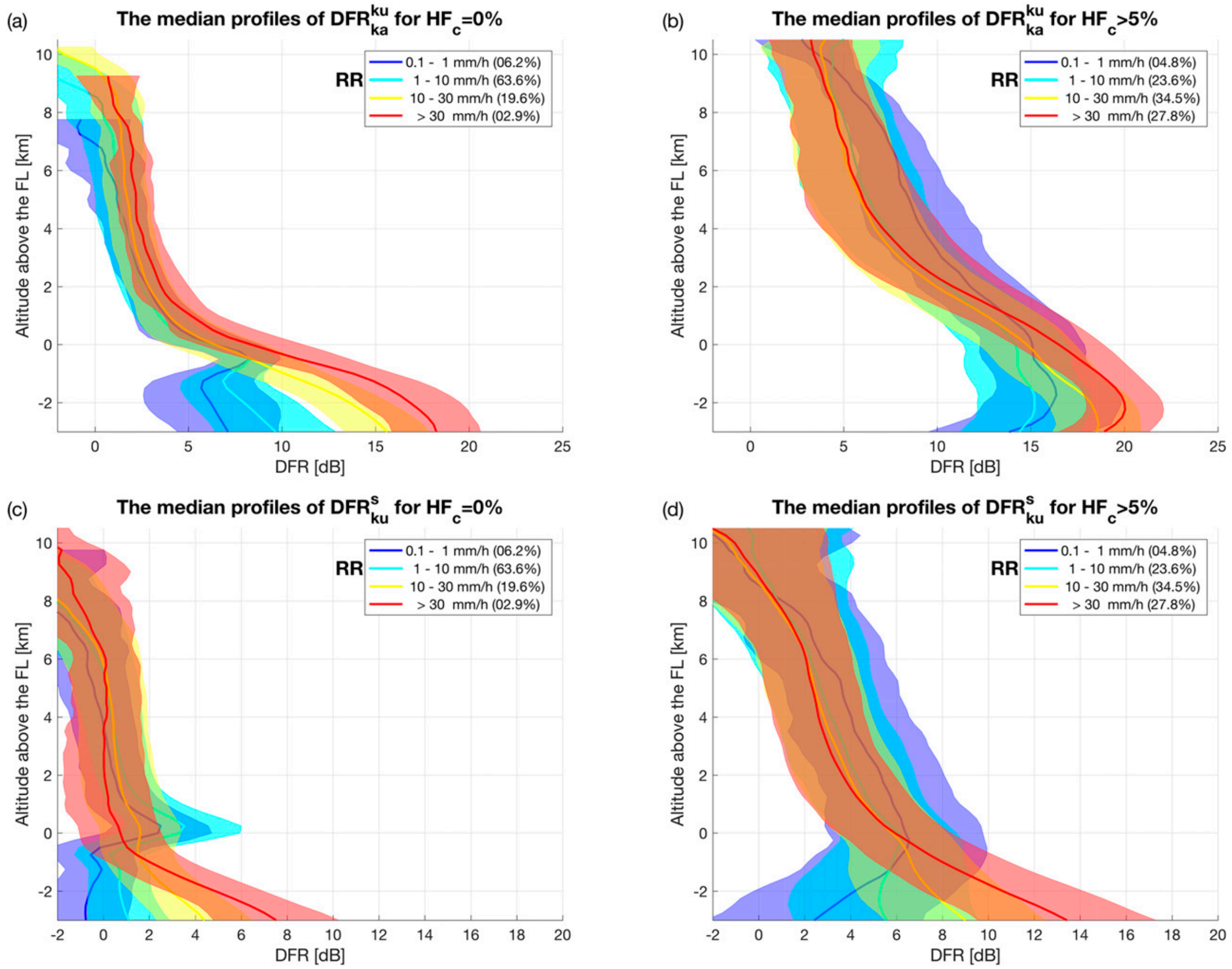

FIG. 5. The median DFR of DPR channels for (a) hail-free and (b) hail-contaminated profiles within the 25th–75th-percentile envelope. (c),(d) The corresponding DFR of S- and Ku-band data. Different colors correspond to different RRs at the ground as derived by NEXRAD (see legend). The frequency of occurrence of each rainfall group is given in the legend.

for hail-free and hail-affected columns are shown in Fig. 5. For hail-free profiles (Fig. 5a), there is a clear correspondence between the RR and the increase in $Z_{\mathrm{Ku}} - Z_{\mathrm{Ka}}$ close to the surface because of differential attenuation and differential scattering effects. This behavior is not observed for hail-contaminated columns (Fig. 5b), where the shape of the DFR profile below the FL does not differ significantly for different rain rates and they are not monotonously increasing with decreasing heights. Since the DFRs are the result of a complex interplay between attenuation, non-Rayleigh, and MS effects, this behavior seems to suggest the presence of MS below the FL. For identifying such columns, the hail-detection algorithm described in Mroz et al. (2017) might be used, whereas the algorithm proposed in Battaglia et al. (2016a) can be used for the quantitative retrieval. For comparison purposes, the median profile of $\mathrm{DFR}^{\mathrm{S}}_{\mathrm{Ku}}$ for hail-free and hail-contaminated columns is also shown. In hail-free conditions (Fig. 5c), differential attenuation effects seem to play the main role with DFR marginally above 0 at the FL, and sharply increasing below it, with the strongest RRs corresponding to the highest values of the $\mathrm{DFR}^{\mathrm{S}}_{\mathrm{Ku}}$ in proximity to the surface. In hail-contaminated profiles, things are more complicated with large DFRs at the FL, likely indicative of non-Rayleigh effects; below the FL, a large increase of DFR may be the result of both non-Rayleigh, for example, caused by melting hailstones (Ryzhkov et al. 2013), and attenuation effects. It is worth noting that the hail-bearing columns associated with the strongest rainfall are characterized by the lowest DFR values above the FL, which indicates low Ku attenuation and weak non-Rayleigh effects characteristic of small hailstones.

All of the abovementioned features derived from DPR measurements can be adapted for estimating the degree of hail contamination. In particular, the height and the strength of the Ka-band reflectivity peak seem to be a good proxy for hail detection. The same can be said about the shape of the DFR profile above the freezing level, for example, for heights between 4 and 8 km, where the sharpest slopes correspond to the highest hail fraction in the column. These hail signatures can feed into the GPM classification module (Le and Chandrasekar 2013) and be potentially used to improve the hail-detection capabilities of the algorithm described by Mroz et al. (2017), but this is beyond the scope of this paper.

2) HAIL AT THE GROUND

More than 1000 of the profiles in our database correspond to hail at the ground. The FL is >3 km above the surface for 440 of them. Because of the small size of the sample, no unequivocal conclusions can be made based on a statistical analysis of the profiles associated with hail fall at the ground. Nevertheless, it is worth noting that the median profile of both DPR channels associated with hail at the ground does not go outside the area restricted by 25th and 75th percentiles of profiles with hail only aloft (not shown). Moreover, a direct inspection of the individual columns has not revealed any distinctive signature of DPR measurements that clearly indicate the presence of hail at the ground. The incapacity of ground hail detection can be attributed to several factors: first, as we have already noted, MS at the Ka band strongly affects measurements below hail shafts; second, detection of hail below the freezing level requires separating the hail contribution to the measured reflectivity from the contribution due to rain, which is a challenging task, per se; and third, strong NUBF induced by the horizontal size of hail shafts drastically complicates the interpretation of the DPR reflectivity profiles (Durden and Tanelli 2008; Short et al. 2013, 2015).

An in-depth inspection of all DPR profiles of deep convective cores in our database led to the discovery of two very similar DPR profiles but corresponding to hail fall and no hail fall at the ground. The first one is from the core of a supercell 240 km west of Dallas, Texas, captured on 2 April 2014 (Fig. 6), whereas the second originates from a convective tower of a squall line 130 km southeast of Dallas observed on 11 May 2015 (Fig. 2). The Ka- and Ku-band measurements look very similar for these two columns (Figs. 6c and 2c). For both, Ku reflectivity reaches 40 dB*Z* at a height of around 12 km and maximal echo of approximately 45 dB*Z* at 10 km; below such altitude, reflectivity remains pretty constant and slowly drops below 40 dB*Z* just above the ground clutter. The DFR is steadily increasing from top to bottom and reaches approximately 20 dB at the ground. Moreover, for both profiles, no surface echo is observed at the Ka band, which indicates very strong attenuation at this channel in either case. The main feature that differentiates these two columns is an extreme Ku-band extinction for the supercell; the signal emerging from the surface is greatly reduced compared to the neighbor profiles (see Fig. 6a). The profile extracted from the squall line has some marks of attenuation at the Ku band, but they are not as strong as in the case of the supercell (Fig. 2a).

On the other hand, the corresponding synthetic S-band measurements reconstructed from high-resolution ground-based observations are very distinct, suggesting completely different hydrometeor composition (Figs. 6c and 2c). The hydrometeor classification indicates heavy hail fall accompanied by shafts of big drops for the first profile (Fig. 6d) and almost 67 dB*Z* at the S band close to the surface, but only rain is identified by the polarimetric classifier for the lowest-elevation scan in the squall line case (Fig. 2d). Moreover, for the supercell profile, hail is a dominant hydrometeor type up to 11 km MSL. In the squall line, the hydrometeor classification algorithm indicates a 50–50 mixture of hail and high-density graupel above the 0°C level (Fig. 2d).

Single-frequency measurements have very limited hail-sizing capabilities; therefore, a triple-frequency retrieval based on an optimal estimation framework is used to provide a better insight of the microphysical properties for the analyzed profiles. In a nutshell, the retrieval combines triple-frequency reflectivity profiles weighted by their respective uncertainty with the background knowledge on the microphysics of the system to provide a physically consistent state of the weather; that is, the following cost function is minimized:

$$\mathrm{CF} = [\mathbf{y} - F(\mathbf{x})]^{\mathrm{T}}\mathbf{S}_m^{-1}[\mathbf{y} - F(\mathbf{x})] + (\mathbf{x} - \mathbf{x}_b)^{\mathrm{T}}\mathbf{S}_b^{-1}(\mathbf{x} - \mathbf{x}_b), \tag{2}$$

where $\mathbf{x}_b$ is the background (priori) knowledge on the retrieved state vector $\mathbf{x}$ whereas $\mathbf{S}_b$ is the background covariance matrix that reflects uncertainty in the estimate of $\mathbf{x}$ prior to the measurement; $\mathbf{y}$ is a vector of measured (and synthetic) reflectivities and F is a forward model operator accounting for attenuation and multiple-scattering effects (Hogan and Battaglia 2008). No correlation between observations is assumed; therefore, the measurement error covariance matrix $\mathbf{S}_m$ has a diagonal form. The DPR reflectivity errors are assumed to be equal to 1 dB, whereas for synthetic S-band data, we followed Turk et al. (2011) and the much bigger uncertainty of 3 dB is used to account for possible temporal/spatial mismatches and the attenuation induced by hydrometeors between the ground-based station and the DPR column. For the retrieval,

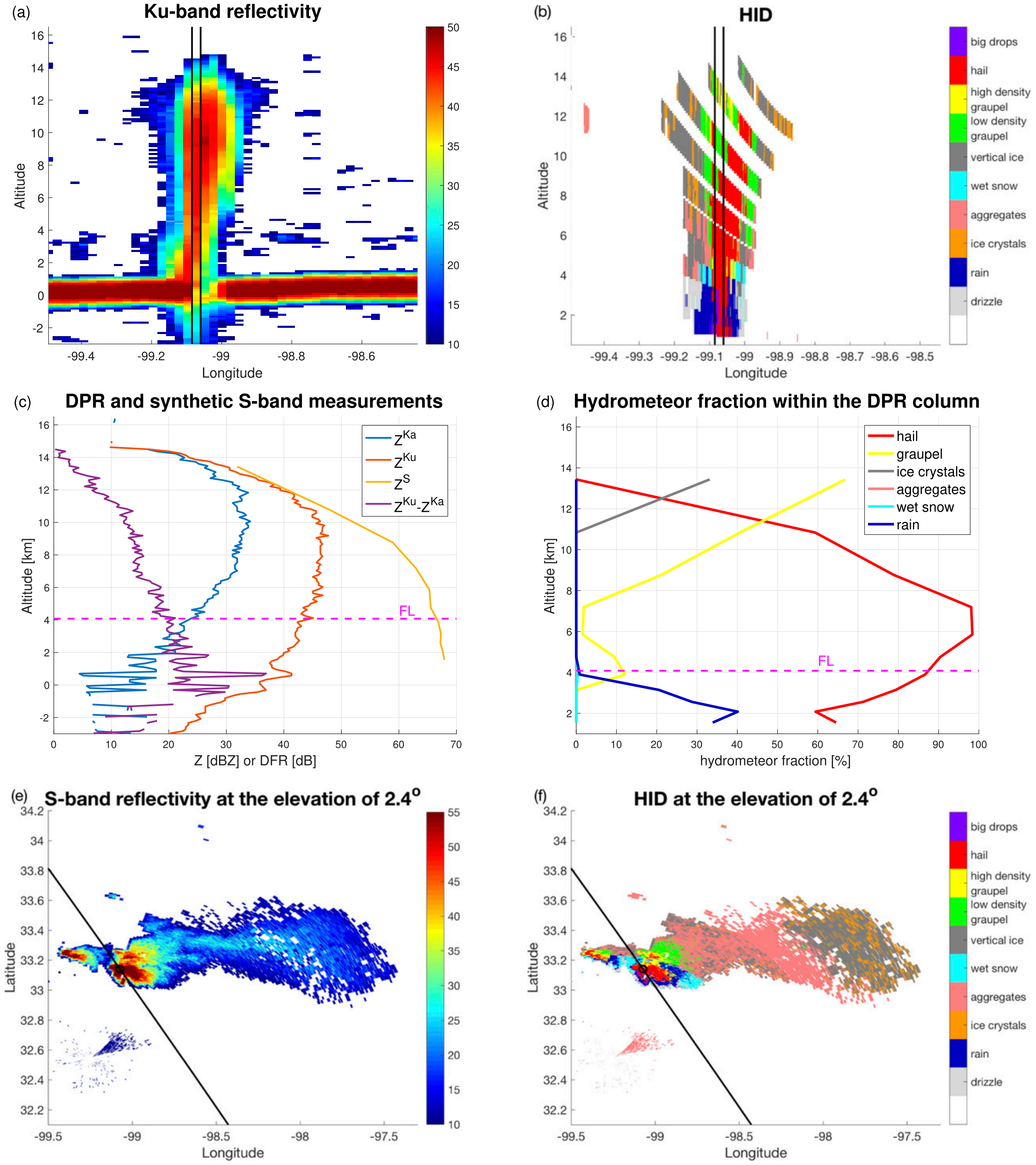

FIG. 6. As in Fig. 2, but for the storm captured on 2 Apr 2014.

we assume that the ice particles are distributed exponentially with respect to size, whereas for rain, the gamma particle size distribution with $\mu = 3$ is used (Liao et al. 2014). The vector of unknowns $\mathbf{x}$ is composed of the mass-weighted mean diameter of particles D_m and the water content. The ground-based hydrometeor classification is utilized to determine the density of ice particles and the position of solid- and liquid-phase hydrometeors in the column. To fully explore the solution space, a range of different a priori assumptions on the unknown vector $\mathbf{x}_b$ is tested. More details on the retrieval can be found in Battaglia et al. (2016a).

The retrieved properties of hydrometeors must be interpreted as a very rough estimate of true microphysical conditions mainly because of the spatial and temporal mismatch of the S-band data. Multifrequency retrievals are very sensitive to any fluctuation in measured reflectivities, and even a small deviation in estimated S-band reflectivity may result in the unrealistic retrieval. Moreover, no attempt to model melting has been made. Despite these limitations, the retrieval provides valuable information on the storm structure. In both cases, high-density particles are retrieved above the freezing level, but the mean mass diameter for the supercell is much bigger than for the squall line (with the maximum value of the mass-weighted mean size peaking at 4 versus 12 mm for altitudes 2 km above the melting level; see Figs. 7c,d). In turn, the ice water content for the squall line was more than twice the value for the supercell and well exceeding 5 g m^{-3} (Figs. 7e,f). Because of the dependence of the extinction coefficients on the mean size of the particle size distribution (Battaglia et al. 2014, Fig. 3 therein), this corresponds to a much larger optical thickness at Ka band for the squall line, with corresponding large values of multiple-scattering enhancements (Fig. 7b).

It is worth noting that the retrieval results suggest that, for the supercell profile, not only Ka- but also Ku-band measurements appear to be partially affected by multiple scattering. The MS enhancement for the Ku-band profile, that is, the difference between the multiple- and single-scattering simulations denoted by continuous and dashed lines in Fig. 7a, is greater than 5 dB for all solutions below the freezing level and is increasing in proximity to the surface. This causes the signal emerging from the volume contaminated by large hail and big drops to look remarkably like the profile with rain only. However, these conclusions may be partially unrealistic because the retrieval assumes a one-dimensional (1D) structure of the storm with no NUBF accounted for. Moreover, assumptions about the hydrometeor shapes and the particle size distribution are made, and all of these uncertainties propagate downward to the surface.

4. Challenges in the interpretation of DPR profiles

The reflectivity measured at the DPR channels results from the weighting according to the antenna pattern of the vertical profiles of attenuated backscattered echo. The inhomogeneity of the backscattering and/or attenuation fields within the DPR footprint can significantly complicate the interpretation of the weighted signal. Additionally, multiple scattering can also significantly affect the reflectivity profiles. Both NUBF and MS effects are very detrimental for quantitative precipitation estimates; as a result, it is highly desirable to be able to flag such conditions.

A new module is being evaluated for integration in the standard DPR level-2 operational algorithm (Tanelli et al. 2017). Dubbed ''trigger'' (because it is designed to trigger different handling of the profile by the ''solver'' module), this module aims at detecting the occurrence of severe MS and NUBF within each DPR footprint in the inner swath (i.e., the matched swath). The trigger algorithm, described in detail in S. Tanelli et al. (2018, unpublished manuscript), performs a series of analyses aimed at detecting the presence or absence of features tied to the presence or absence of NUBF and MS:

1) variability of the measured reflectivity at the Ka band of neighboring profiles from matching and high-sensitivity swaths to provide a robust estimate of the inhomogeneity of a footprint; this analysis includes two independent metrics: the fraction of footprint estimated to have no detectable scattering and the standard deviation of the reflectivity where scattering is detected;
2) departure of the ratio of path-integrated attenuation (PIA) at Ka band versus PIA at Ku band from the expected range (see Durden and Tanelli 2008; Tanelli et al. 2012, and references therein);
3) presence or absence of a visible peak attributed to Earth's surface (Battaglia and Simmer 2008);
4) presence or absence of an MS ''tail'' through the surface (Battaglia et al. 2010); and
5) presence or absence of a ''deep'' DFR knee (Battaglia et al. 2014).

These feature detections are combined with a few conservative thresholds on the maxima of reflectivity and are analyzed contextually to provide an estimate of occurrence of each of the two phenomena. The presence of MS is summarized in one detection flag that can assume three values (0 = absent, 100 = present, 50 = possibly present/uncertain). While a similar flag is created for NUBF, its use is less relevant since the presence of a certain degree of NUBF is quite ubiquitous; however, it is of use in preliminary assessments regarding the presence of significant nonuniformity that would bias the retrievals by amounts much larger than the intrinsic product uncertainty. An example of the output of the trigger, corresponding to the case study depicted in Fig. 2, is shown in Fig. 8a. As a reference, the horizontal structure of the storm captured by the maximum Ku reflectivity in the column is presented in Fig. 8b.

To cluster the outputs of the trigger, a hierarchy of hydrometeor types is used to attribute a ''dominant'' hydrometeor class in the column. First, the maximal

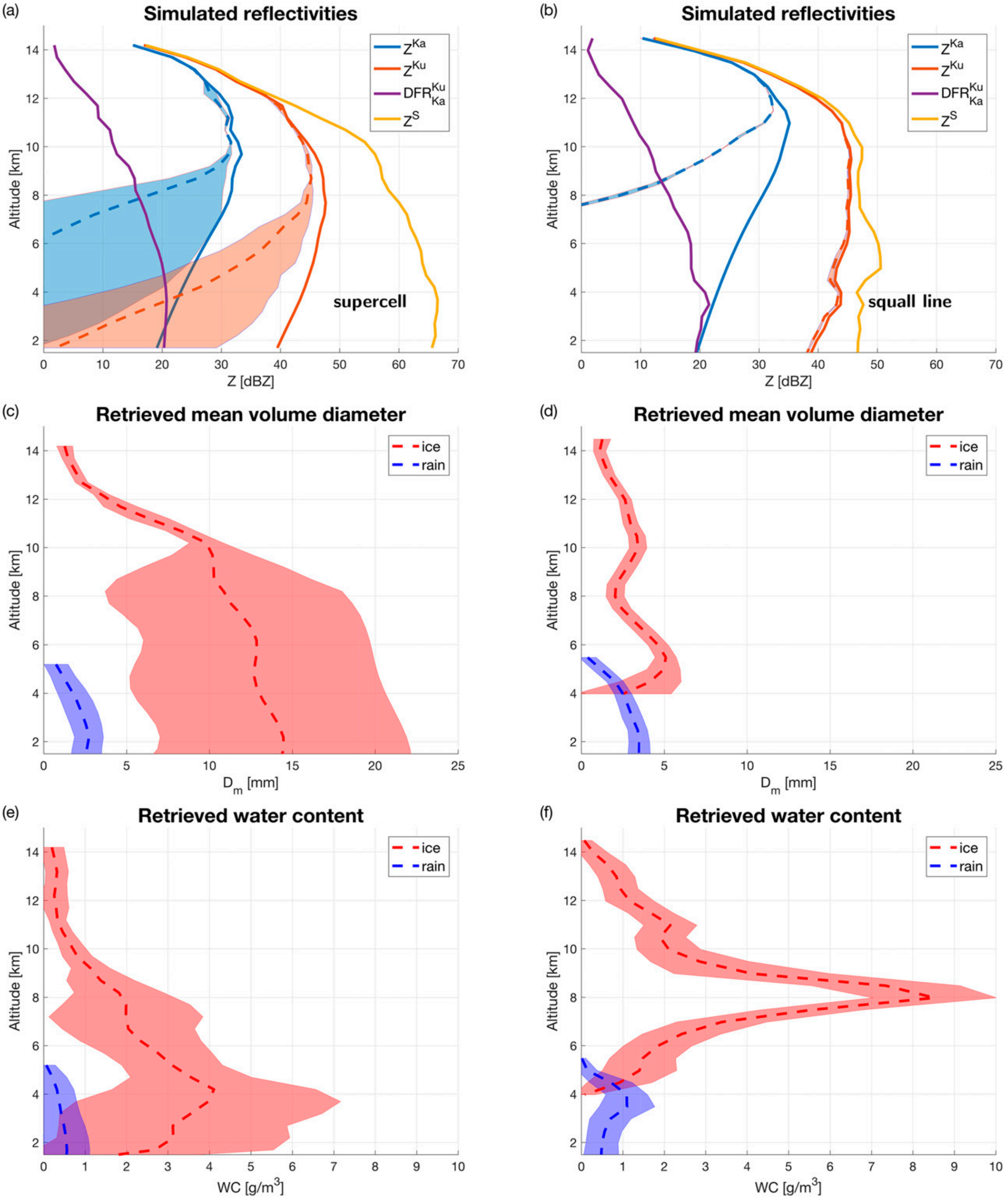

FIG. 7. Triple-frequency simulated reflectivities of the columns associated with (a) hail falling at the ground and with (b) hail only aloft. Continuous (dashed) lines correspond to reflectivities with all orders of scattering (only single scattering) included. The continuous lines match very well the observations that are depicted in Fig. 6c and Fig. 2c, respectively. The colors represent different frequency simulations (see legend). (c),(d) The triple-frequency retrieved mean volume diameter of ice (red) and rain (blue) corresponding to measurements shown in (a) and (b), respectively. (e),(f) As in (c) and (d), but the water content is presented. The dashed lines show the median profile, whereas the shaded area represents the spread between 10th and 90th percentiles of all converging solutions. In (a) and (b), the spread of single-scattering simulated reflectivities is presented.

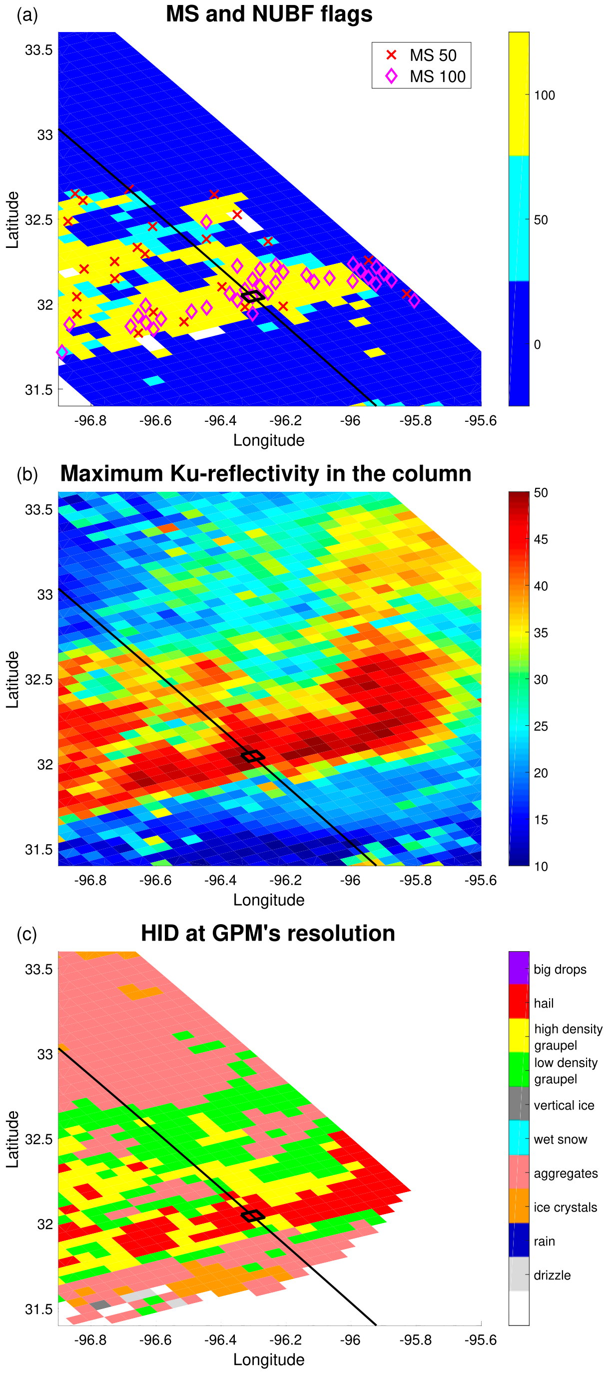

FIG. 8. (a) The output of the trigger algorithm for the storm shown in Fig. 2. The NUBF flag is represented by different colors, whereas the MS flag is shown by different markers as described in the legend. (b) The maximum Ku reflectivity in the column. (c) The "dominant" hydrometeor type in the column as derived from the ground-based polarimetric classification algorithm. The black line and the black rectangle show the location of the cross section and the profile shown in Figs. 2a and 2c, respectively.

TABLE 2. The percentage of hail- and graupel-bearing columns flagged by the trigger algorithm as MS or NUBF affected. The percentage of profiles within the three different classes over all profiles in the database is given in the parentheses.

	NUBF 0	NUBF 50	NUBF 100
Hail (3.2%)			
MS 0	22.7	10.5	38.0
MS 50	2.3	1.6	6.7
MS 100	2.5	2.0	13.7
High-density graupel (6.1%)			
MS 0	68.1	10.6	7.4
MS 50	5.0	1.4	1.1
MS 100	4.1	1.1	1.1
Low-density graupel (15.9%)			
MS 0	93.4	1.0	0.3
MS 50	3.5	0.1	0.0
MS 100	1.6	0.1	0.0

fraction of the DPR footprint of each hydrometeor type is calculated in the column, then the species that occupies more than 5% of the footprint with the highest priority is used as a dominant type. The hierarchy of hydrometeor classes in descending order is as follows: hail, high- and low-density graupel, aggregates, ice crystals, and, finally, a group that combines all liquid-phase particles. In this way, profiles dominated by hail are those where $HF_c > 5\%$. The output of this procedure applied to the high-resolution ground-based data for the storm from Fig. 2 is shown in Fig. 8c.

Table 2 shows the probability of NUBF and MS flags for three dominant hydrometer types. As much as 58% of the DPR profiles contaminated with hail are strongly affected by NUBF. Extreme nonuniform effects are much less common among profiles occupied by high-density graupel (10%) and occur only occasionally for low-density graupel (0.03%). Moderate NUBF is observed for 14% of profiles dominated by hail. The same level of inhomogeneity is detected for 13% and 1% of columns occupied by high- and low-density graupel, respectively. Signatures of severe MS are observed less frequently than signatures of NUBF; an MS warning (MS50 or MS100) is only issued for 29%, 14%, and 5% of columns contaminated with hail and high- and low-density graupel, respectively. The fraction of hail-contaminated profiles affected by MS increases with increasing hail fraction, reaching about 90% for profiles fully filled with hail (not shown). On the other hand, most of the profiles affected by MS (61%) are occupied by graupel. This is somehow expected because the total number of profiles filled with graupel is about 5 times larger than the number of hail-bearing columns. It demonstrates that the signatures of extreme MS are not a peculiarity of profiles containing high-density particles but

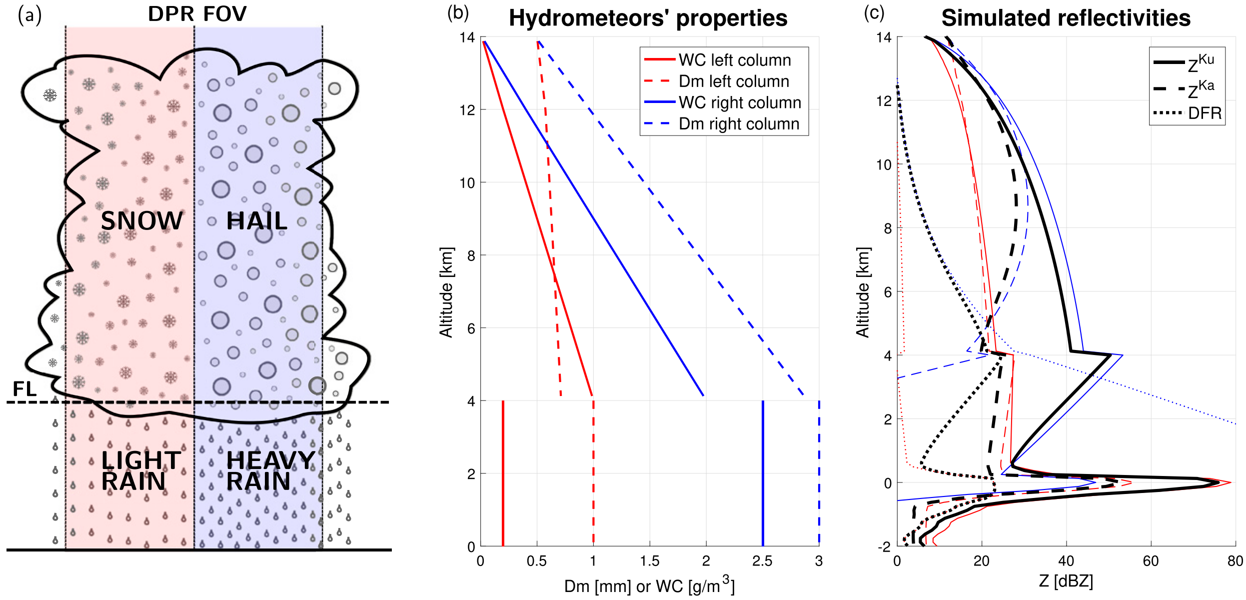

FIG. 9. (a) Schematic of a conceptual model used in our simulations. The red part is occupied by low-density aggregates and, below the FL, by light rain. The blue volume is filled with hail and is associated with heavy rainfall underneath. (b) The microphysical properties of the hydrometeors used in our simulations. The red (blue) line corresponds to the half of the DPR volume marked by the same color. (c) The DPR measurements of the modeled convective system. Again, the color coding reflects the origin of sampling. The black lines denote the measurements of the full volume.

can also occur in the presence of a heavy load of relatively small ice particles.

As mentioned before, one of the two criteria for the detection of MS in the trigger is the presence of a DFR knee. The underlying assumption is that the knee is an unequivocal signature of MS. The mechanism for the MS generation of the knee is illustrated by the schematic in Fig. 4 of Battaglia et al. (2015). In a nutshell, a DFR knee occurs when the attenuation due to rain or hail at the higher-frequency channel is partially compensated by multiple-scattered radiation aloft. In the presence of considerable MS, this reflectivity enhancement can alter the reflectivity at the higher frequency to a level such that the decrease of Z with range becomes larger at the lower frequency. This explanation is based on the assumption that the radar volume is uniformly filled. However, such an assumption may not be valid for convective cells that are usually smaller than the DPR footprint (20 km^2). DFR knees can indeed appear in association with strong NUBF as well.

Consider a conceptual model assuming an exponential particle size distribution for rain and ice where the DPR volume is split into two equal parts. One-half above the FL is filled by snow and small ice crystals, and the other is occupied by hail. Below the FL, heavy and light rain shafts are adjacent to each other (see Fig. 9a) with heavy precipitation underneath the hail column. The corresponding profiles of the mean volume melted diameter and the water content are shown in Fig. 9b. No attempt to model any melting has been made, so the results around the FL may look unrealistic.

The single-scattering assumption is used to model DPR reflectivities. Figure 9c shows simulated Ka- and Ku-band reflectivities corresponding to each part of the volume. The blue (red) lines correspond to the part occupied by hail (snow). The simulated reflectivities as measured by the DPR (black lines) are obtained as the mean of the two reflectivities (expressed in linear units):

$$Z_{\mathrm{DPR}} = 0.5(Z_{\mathrm{red\_volume}} + Z_{\mathrm{blue\_volume}}). \qquad (3)$$

Although the measurements in each part are characterized by an almost monotonic increase of DFR from top to bottom (red and blue dotted lines in Fig. 9c), the reflectivity that corresponds to the full volume is characterized by a DFR knee (black dotted line). The knee appears because the signals sensed by two radars below the FL are dominated by different processes. The column of hail strongly attenuates the Ka channel (dashed blue line); therefore, the radiation backscattered from the light rain located below the low-attenuating medium (dashed red line) controls the behavior of the Ka-band signal in the full volume below the FL with the total signal converging to half (or 3 dB less than) the red signal. On the other hand, the shape of the Ku-band reflectivity is driven by the column of hail aloft and by the heavy rain shaft underneath (continuous blue line) because they are several orders of magnitude more reflective than snow or light rain. This conceptual example urges caution in the interpretation of DFR knees as an incontrovertible signature of multiple scattering.

The trigger algorithm is inherently capable of capturing these situations. In fact, the profile depicted in Fig. 9 shows strong NUBF signatures as highlighted by the strength of the Ku and Ka surface profile. Such profiles have been simulated based on the shape of GPM DPR ocean surface reflectivity profiles at nadir in the presence of clear-sky conditions for a full orbit (orbit number 6806) and accounting for the PIAs at Ku and Ka. The clear-sky surface peaks at 79.3 and 61.2 dB*Z* are reduced to 75.8 and 53.1 dB*Z* for Ku and Ka, respectively. At Ku, the PIA that would be measured via the surface reference technique (SRT) would be 3.5 dB, marginally higher than 3 dB (i.e., a factor of 2), practically signaling that half of the footprint is fully attenuating and the other half is barely producing any attenuation. Because of 5 dB of attenuation produced by the snow-bearing column, the Ka SRT PIA adds up to 8.1 dB. Therefore, the ratio of the two path-integrated attenuations ($\mathrm{PIA}_{\mathrm{Ka}}/\mathrm{PIA}_{\mathrm{Ku}}$) is equal to 2.3, which is well below the trigger NUBF detection threshold of 4. Therefore, this profile would be marked as affected by both NUBF and MS.

An example of the real DPR measurements associated with the NUBF knee is presented in Fig. 10 for a multicell system observed on 17 May 2016 offshore of Miami, Florida. The DPR signal exhibits strong signatures of MS, that is, high Ku reflectivity values (more than 40 dB*Z*) and the DFR knee exceeding 20 dB in amplitude (Fig. 10a), but at the same time, the SRT PIA at the Ka band does not exceed 5 dB (see Fig. 10c), much less than is necessary for significant MS to occur. The variability of the PIA field in the neighborhood of the profile clearly indicates inhomogeneity within the column: two of the "high sensitivity" scans that partially overlap with the profile of interest are characterized by very low attenuation, whereas for the other two, the PIA exceeds 15 dB. The high-resolution ground-based data (see Fig. 10b), confirm what the SRT PIA suggests; that is, half of the DPR volume (black circle) is filled by highly reflective ($Z > 45$ dB*Z*) and strongly attenuating particles, whereas the other part is occupied by hydrometeors characterized by much smaller backscattering. This is exactly the scenario described in the conceptual model where the slopes of the Ku and Ka reflectivity in rain are uncorrelated because two DPR channels are sensitive to different parts of the footprint, and therefore, the DFR knee is deemed to be caused by NUBF more than MS.

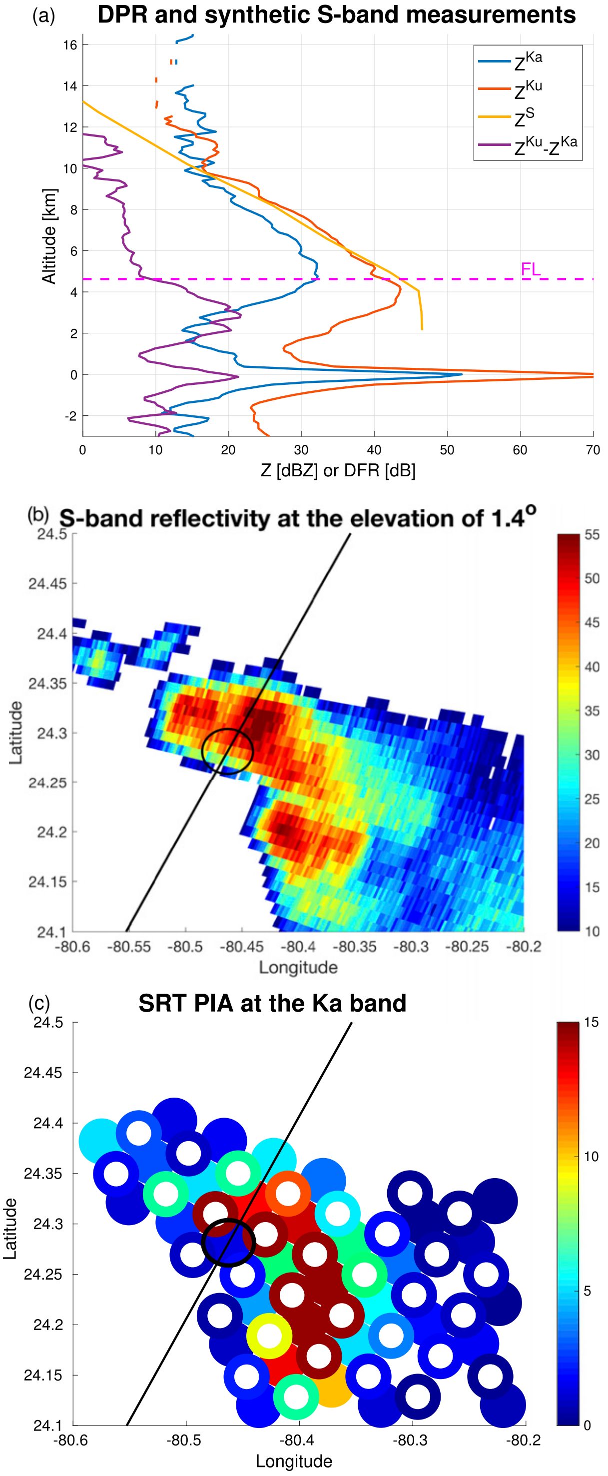

FIG. 10. An example of DPR measurements associated with the DFR knee and strong NUBF. The depicted storm was observed on 17 May 2016 offshore of Miami. (a) DPR observables supplemented by the corresponding synthetic S-band reflectivity profile. (b) Ground-based radar measurements at the low-elevation angle at the native resolution. (c) PIA estimate at the Ka band based on the SRT. Disks and circles correspond to the measurements within matching and high-sensitivity swaths, respectively. The black circle in (b) and (c) marks the horizontal position of the columnar measurements in (a).

5. Summary

A statistical analysis of the Dual-Frequency Precipitation Radar (DPR) measurements of hail-bearing profiles is thoroughly described throughout this paper. The analysis conducted here relies on simultaneous observations from the Next Generation Weather Radar (NEXRAD) network in the United States and from the Global Precipitation Measurement (GPM) mission *Core Observatory*. High-resolution measurements within a 100-km proximity to the ground-based stations are used to characterize the variability within the DPR pixels. For hail detection, the polarimetric identification of hydrometeors, not ground reports, is utilized as truth. ‘‘Hail fall at the ground’’ is identified when hail is detected in the lowest-elevation radar scan.

The analysis shows that the probability of finding hail within convective systems is very small. About 41% of all profiles exceeding the 40-dB*Z* Ku reflectivity threshold have no hail in the column, and for only 26% of them, hail occupies an area exceeding 1 km^2 at some altitude level. The chance of capturing hail fall at the ground is even smaller. Most hail-contaminated profiles (74%) are associated with pure rainfall underneath, and only 9% of them are characterized by a hail fall area bigger than 1 km^2. Because the detection of hail at the ground is based on the lowest-elevation radar data, the number of profiles with hail truly reaching the ground may be even smaller because of melting. The probability of hail at the ground is inversely proportional to the freezing-level height. Our database does not include a single DPR profile that is uniformly filled by hail in proximity to the surface (the DPR footprint size is about 20 km^2). The structure of convective storms is very inhomogeneous: hail shafts below the freezing level typically coexist with rain, which makes it very challenging to correctly interpret dual-frequency measurements.

The DPR measurements of columns contaminated with hail, exclusively above the ground, differ significantly from those columns that are hail free. The peak Ka reflectivity value occurs above the freezing level (FL), and its height is proportional to the maximum fraction of the DPR FOV occupied by hail at any level. Moreover, stronger Ku-band echoes are observed for higher hail contamination. In terms of dual-frequency ratio (DFR), bigger differences in measured reflectivities above the FL are observed for higher hail fractions. These distinctive features of DPR measurements of hail-bearing columns (see Fig. 4) can be potentially used to enhance existing hail-detection routines; for example, see Ni et al. (2017) and Mroz et al. (2017). Stronger hail contamination amplifies multiple scattering (MS) at the Ka band, which is manifested in abnormal sloping of the DFR profile below the freezing level. This is likely to affect the accuracy of DPR rain rates’ estimates.

The interpretation of DPR measurements of hail-bearing columns, in particular the detection of hail at the ground, remains a very challenging problem. The presence of hail aloft strongly affects Ka-band measurements not only by attenuation but also by MS. Both effects amplify uncertainty in the effective reflectivity estimates below the freezing level, which in this region effectively reduces the DPR measurements to the Ku channel only. Because single-frequency observations provide very limited sizing information, the potential for the detection of hailstones at the surface is greatly hampered in MS-contaminated columns.

The presence of a DFR ‘‘knee’’ should not be interpreted as an incontrovertible signature of MS. In some instances, NUBF may also produce DFR knees similar to those expected from MS effects, as is clearly illustrated in Fig. 9, where a part of the instrument FOV is occupied by particles that strongly attenuate only one of the DPR channels. In case of a DFR knee, a check of the strength of the surface return at the Ka band might be useful in distinguishing MS from NUBF effects—with the latter being dominant corresponding to a clear surface return peak (Tanelli et al. 2005).

The signatures of extreme MS, as detected by the trigger algorithm, are the most commonly observed among hail-bearing profiles—with 29% of them flagged as severely affected. Nevertheless, MS is not characteristic only to hail-contaminated columns. The profiles filled by less-rimed particles, like graupel, are also affected but to a smaller degree; that is, 14% and 5% of profiles occupied by high- and low-density graupel show signatures of MS, respectively. On the other hand, more than 61% of all MS-affected columns (according to the trigger) are filled with graupel, which is due to the fact that the occurrence of graupel is much more common: the number of hail-bearing columns is approximately 5 times smaller than the number of profiles filled with graupel. Nevertheless, it is likely that some of the graupel-bearing columns identified as being affected by MS, based on the occurrence of the DFR knee, have signatures caused by NUBF instead. According to the trigger, 22% of the profiles characterized by a DFR knee (one of the MS signatures) are affected by strong NUBF (NUBF flag = 100). However, a DFR knee is observed for only 25% of all profiles strongly affected by MS, which indicates that DFR knees are not the unique MS signatures.

Our analysis reveals that most of the DPR profiles that are contaminated with either hail or high-density graupel are affected by extreme NUBF. As much as 84% and 62% of hail- or graupel-bearing columns have the highest NUBF flag level, as detected by the trigger algorithm. Strong inhomogeneity is less common among profiles filled by low-density graupel (16%) or aggregates (<3%). In light of these findings, future spaceborne radar-based missions oriented at observing deep convective cores should aim at finer horizontal resolution than currently achieved with the GPM DPR.

Acknowledgments. The work done by A. Battaglia was funded by the project ''Calibration and validation studies over the North Atlantic and United Kingdom for the Global Precipitation Mission'' funded by the U.K. NERC (NE/L007169/1). Timothy Lang was funded by the GPM Ground Validation program, under the direction of Mathew Schwaller and Ramesh Kakar of the National Aeronautics and Space Administration. The work by Simone Tanelli and Gian Franco Sacco was performed at the Jet Propulsion Laboratory, California Institute of Technology, under contract with the National Aeronautics and Space Administration in support to the Precipitation Measurement Missions Science Team. Level-2, V05, GPM data were downloaded from the Precipitation Processing System. NEXRAD data were downloaded from the National Oceanic and Atmospheric Administration National Climatic Data Center and were processed using the following open source packages: Py-ART, CSU_RadarTools, DualPol, SkewT, and ARTview. This research used the SPECTRE High Performance Computing Facility at the University of Leicester.

REFERENCES

Auer, A. H., Jr., 1994: Hail recognition through the combined use of radar reflectivity and cloud-top temperatures. *Mon. Wea. Rev.*, **122**, 2218–2221, https://doi.org/10.1175/1520-0493(1994)122<2218:HRTTCU>2.0.CO;2.

Baldini, L., V. Chandrasekar, and D. Moisseev, 2012: Microwave radar signatures of precipitation from S band to K_a band: Application to GPM mission. *Eur. J. Remote Sens.*, **45**, 75–88, https://doi.org/10.5721/EuJRS20124508.

Battaglia, A., and C. Simmer, 2008: How does multiple scattering affect the spaceborne W-band radar measurements at ranges close to and crossing the sea-surface range? *IEEE Trans. Geosci. Remote Sens.*, **46**, 1644–1651, https://doi.org/10.1109/TGRS.2008.916085.

——, S. Tanelli, S. Kobayashi, D. Zrnic, R. J. Hogan, and C. Simmer, 2010: Multiple-scattering in radar systems: A review. *J. Quant. Spectrosc. Radiat. Transfer*, **111**, 917–947, https://doi.org/10.1016/j.jqsrt.2009.11.024.

——, ——, G. M. Heymsfield, and L. Tian, 2014: The dual wavelength ratio knee: A signature of multiple scattering in airborne Ku–Ka observations. *J. Appl. Meteor. Climatol.*, **53**, 1790–1808, https://doi.org/10.1175/JAMC-D-13-0341.1.

——, ——, K. Mroz, and F. Tridon, 2015: Multiple scattering in observations of the GPM Dual-Frequency Precipitation Radar: Evidence and impact on retrievals. *J. Geophys. Res. Atmos.*, **120**, 4090–4101, https://doi.org/10.1002/2014JD022866.

——, K. Mroz, T. Lang, F. Tridon, S. Tanelli, L. Tian, and G. M. Heymsfield, 2016a: Using a multiwavelength suite of microwave instruments to investigate the microphysical structure of deep convective cores. *J. Geophys. Res. Atmos.*, **121**, 9356–9381, https://doi.org/10.1002/2016JD025269.

——, ——, S. Tanelli, F. Tridon, and P.-E. Kirstetter, 2016b: Multiple-scattering-induced ''ghost echoes'' in GPM DPR observations of a tornadic supercell. *J. Appl. Meteor. Climatol.*, **55**, 1653–1666, https://doi.org/10.1175/JAMC-D-15-0136.1.

Bringi, V. N., and V. Chandrasekar, 2001: *Polarimetric Doppler Weather Radar: Principles and Applications.* Cambridge University Press, 636 pp.

Cecil, D. J., 2009: Passive microwave brightness temperatures as proxies for hailstorms. *J. Appl. Meteor. Climatol.*, **48**, 1281–1286, https://doi.org/10.1175/2009JAMC2125.1.

——, 2011: Relating passive 37-GHz scattering to radar profiles in strong convection. *J. Appl. Meteor. Climatol.*, **50**, 233–240, https://doi.org/10.1175/2010JAMC2506.1.

——, and C. B. Blankenship, 2012: Toward a global climatology of severe hailstorms as estimated by satellite passive microwave imagers. *J. Climate*, **25**, 687–703, https://doi.org/10.1175/JCLI-D-11-00130.1.

Depue, T. K., P. C. Kennedy, and S. A. Rutledge, 2007: Performance of the hail differential reflectivity (H_{DR}) polarimetric radar hail indicator. *J. Appl. Meteor. Climatol.*, **46**, 1290–1301, https://doi.org/10.1175/JAM2529.1.

Dolan, B., and S. A. Rutledge, 2009: A theory-based hydrometeor identification algorithm for X-band polarimetric radars. *J. Atmos. Oceanic Technol.*, **26**, 2071–2088, https://doi.org/10.1175/2009JTECHA1208.1.

——, ——, S. Lim, V. Chandrasekar, and M. Thurai, 2013: A robust C-band hydrometeor identification algorithm and application to a long-term polarimetric radar dataset. *J. Appl. Meteor. Climatol.*, **52**, 2162–2186, https://doi.org/10.1175/JAMC-D-12-0275.1.

Donaldson, R. J., Jr., 1959: Analysis of severe convective storms observed by radar—II. *J. Meteor.*, **16**, 281–287, https://doi.org/10.1175/1520-0469(1959)016<0281:AOSCSO>2.0.CO;2.

Durden, S. L., and S. Tanelli, 2008: Predicted effects of nonuniform beam filling on GPM radar data. *IEEE Geosci. Remote Sens. Lett.*, **5**, 308–310, https://doi.org/10.1109/LGRS.2008.916068.

Ferraro, R., J. Beauchamp, D. Cecil, and G. Heymsfield, 2015: A prototype hail detection algorithm and hail climatology developed with the Advanced Microwave Sounding Unit (AMSU). *Atmos. Res.*, **163**, 24–35, https://doi.org/10.1016/j.atmosres.2014.08.010.

Heinselman, P. L., and A. V. Ryzhkov, 2006: Validation of polarimetric hail detection. *Wea. Forecasting*, **21**, 839–850, https://doi.org/10.1175/WAF956.1.

Hogan, R. J., and A. Battaglia, 2008: Fast lidar and radar multiple-scattering models. Part II: Wide-angle scattering using the time-dependent two-stream approximation. *J. Atmos. Sci.*, **65**, 3636–3651, https://doi.org/10.1175/2008JAS2643.1.

Hou, A. Y., and Coauthors, 2014: The Global Precipitation Measurement Mission. *Bull. Amer. Meteor. Soc.*, **95**, 701–722, https://doi.org/10.1175/BAMS-D-13-00164.1.

Kitzmiller, D. H., W. E. McGovern, and R. F. Saffle, 1995: The WSR-88D severe weather potential algorithm. *Wea. Forecasting*, **10**, 141–159, https://doi.org/10.1175/1520-0434(1995)010<0141:TWSWPA>2.0.CO;2.

Kozu, T., and T. Iguchi, 1999: Nonuniform beamfilling correction for spaceborne radar rainfall measurement: Implications from TOGA COARE radar data analysis. *J. Atmos. Oceanic Technol.*, **16**, 1722–1735, https://doi.org/10.1175/1520-0426(1999)016<1722:NBCFSR>2.0.CO;2.

Kummerow, C., W. Barnes, T. Kozu, J. Shiue, and J. Simpson, 1998: The Tropical Rainfall Measuring Mission (TRMM) sensor package. *J. Atmos. Oceanic Technol.*, **15**, 809–817, https://doi.org/10.1175/1520-0426(1998)015<0809:TTRMMT>2.0.CO;2.

Le, M., and V. Chandrasekar, 2013: Precipitation type classification method for Dual-Frequency Precipitation Radar (DPR) onboard the GPM. *IEEE Trans. Geosci. Remote Sens.*, **51**, 1784–1790, https://doi.org/10.1109/TGRS.2012.2205698.

Leppert, K. D., II, and D. J. Cecil, 2015: Signatures of hydrometeor species from airborne passive microwave data for frequencies 10–183 GHz. *J. Appl. Meteor. Climatol.*, **54**, 1313–1334, https://doi.org/10.1175/JAMC-D-14-0145.1.

Liao, L., R. Meneghini, and A. Tokay, 2014: Uncertainties of GPM DPR rain estimates caused by DSD parameterizations. *J. Appl. Meteor. Climatol.*, **53**, 2524–2537, https://doi.org/10.1175/JAMC-D-14-0003.1.

Marra, A. C., and Coauthors, 2017: Observational analysis of an exceptionally intense hailstorm over the Mediterranean area: Role of the GPM Core Observatory. *Atmos. Res.*, **192**, 72–90, https://doi.org/10.1016/j.atmosres.2017.03.019.

Meneghini, R., and L. Liao, 2013: Modified Hitschfeld–Bordan equations for attenuation-corrected radar rain reflectivity: Application to nonuniform beamfilling at off-nadir incidence. *J. Atmos. Oceanic Technol.*, **30**, 1149–1160, https://doi.org/10.1175/JTECH-D-12-00192.1.

Mroz, K., A. Battaglia, T. J. Lang, D. J. Cecil, S. Tanelli, and F. Tridon, 2017: Hail-detection algorithm for the GPM core satellite sensors. *J. Appl. Meteor. Climatol.*, **56**, 1939–1957, https://doi.org/10.1175/JAMC-D-16-0368.1.

Musil, D. J., S. A. Christopher, R. A. Deola, and P. L. Smith, 1991: Some interior observations of southeastern Montana hailstorms. *J. Appl. Meteor.*, **30**, 1596–1612, https://doi.org/10.1175/1520-0450(1991)030<1596:SIOOSM>2.0.CO;2.

Nesbitt, S. W., E. J. Zipser, and D. J. Cecil, 2000: A census of precipitation features in the tropics using TRMM: Radar, ice scattering, and lightning observations. *J. Climate*, **13**, 4087–4106, https://doi.org/10.1175/1520-0442(2000)013<4087:ACOPFI>2.0.CO;2.

Ni, X., C. Liu, D. J. Cecil, and Q. Zhang, 2017: On the detection of hail using satellite passive microwave radiometers and Precipitation Radar. *J. Appl. Meteor. Climatol.*, **56**, 2693–2709, https://doi.org/10.1175/JAMC-D-17-0065.1.

Ortega, K. L., T. M. Smith, K. L. Manross, K. A. Scharfenberg, A. Witt, A. G. Kolodziej, and J. J. Gourley, 2009: The Severe Hazards Analysis and Verification Experiment. *Bull. Amer. Meteor. Soc.*, **90**, 1519–1530, https://doi.org/10.1175/2009BAMS2815.1.

——, J. M. Krause, and A. V. Ryzhkov, 2016: Polarimetric radar characteristics of melting hail. Part III: Validation of the algorithm for hail size discrimination. *J. Appl. Meteor. Climatol.*, **55**, 829–848, https://doi.org/10.1175/JAMC-D-15-0203.1.

Ryzhkov, A. V., and D. S. Zrnić, 1995: Comparison of dual-polarization radar estimators of rain. *J. Atmos. Oceanic Technol.*, **12**, 249–256, https://doi.org/10.1175/1520-0426(1995)012<0249:CODPRE>2.0.CO;2.

——, M. R. Kumjian, S. M. Ganson, and A. P. Khain, 2013: Polarimetric radar characteristics of melting hail. Part I: Theoretical simulations using spectral microphysical modeling. *J. Appl. Meteor. Climatol.*, **52**, 2849–2870, https://doi.org/10.1175/JAMC-D-13-073.1.

Short, D., K. Nakagawa, and T. Iguchi, 2013: Reduction of nonuniform beam filling effects by vertical decorrelation: Theory and simulations. *J. Meteor. Soc. Japan*, **91**, 539–543, https://doi.org/10.2151/jmsj.2013-408.

——, R. Meneghini, A. E. Emory, and M. R. Schwaller, 2015: Reduction of nonuniform beamfilling effects by multiple constraints: A simulation study. *J. Atmos. Oceanic Technol.*, **32**, 2114–2124, https://doi.org/10.1175/JTECH-D-15-0021.1.

Tanelli, S., S. Durden, and E. Im, 2005: Characterization of Ka- and Ku-band sea surface backscatter for GPM radar applications. JPL, http://hdl.handle.net/2014/38546.

——, G. F. Sacco, S. L. Durden, and Z. S. Haddad, 2012: Impact of non-uniform beam filling on spaceborne cloud and precipitation radar retrieval algorithms. *Proc. SPIE*, **8523**, 852308, https://doi.org/10.1117/12.977375.

——, ——, A. Battaglia, P.-E. Kirstetter, and J. Kwiatkowski, 2017: The trigger algorithm for DPR detection of NUBF and multiple scattering: Validation. JPL, https://pmm.nasa.gov/sites/default/files/meeting_files/PMM%20Science%20Team%20Meeting%202017/Posters/220Tanelli.pdf.

Turk, F. J., K.-W. Park, Z. S. Haddad, P. Rodriguez, and D. R. Hudak, 2011: Constraining CloudSat-based snowfall profiles using surface observations and C-band ground radar. *J. Geophys. Res.*, **116**, D23205, https://doi.org/10.1029/2011JD016126.

Waldvogel, A., B. Federer, and P. Grimm, 1979: Criteria for the detection of hail cells. *J. Appl. Meteor.*, **18**, 1521–1525, https://doi.org/10.1175/1520-0450(1979)018<1521:CFTDOH>2.0.CO;2.

Witt, A., M. D. Eilts, G. J. Stumpf, J. T. Johnson, E. D. W. Mitchell, and K. W. Thomas, 1998: An enhanced hail detection algorithm for the WSR-88D. *Wea. Forecasting*, **13**, 286–303, https://doi.org/10.1175/1520-0434(1998)013<0286:AEHDAF>2.0.CO;2.

Zipser, E. J., D. J. Cecil, C. Liu, S. W. Nesbitt, and D. P. Yorty, 2006: Where are the most intense thunderstorms on Earth? *Bull. Amer. Meteor. Soc.*, **87**, 1057–1072, https://doi.org/10.1175/BAMS-87-8-1057.